Low-temperature selective catalytic reduction of NO with NH$_3$ over an FeO$_x$/β-MnO$_2$ composite

Bo Du,[abc] Yuting Hu,[abc] Ting Cheng,[abc] Zhaozhong Jiang,[abc] Zhenzhen Wang[abc] and Chengzhu Zhu ✩*[abcd]

A series of Fe-modified β-MnO$_2$ (FeO$_x$/β-MnO$_2$) composite catalysts were prepared by an impregnation method with β-MnO$_2$ and ferro nitrate as raw materials. The structures and properties of the composites were systematically characterized and analyzed by X-ray diffraction, N$_2$ adsorption–desorption, high-resolution electron microscopy, temperature-programmed reduction of H$_2$, temperature-programmed desorption of NH$_3$, and FTIR infrared spectroscopy. The deNO$_x$ activity, water resistance, and sulfur resistance of the composite catalysts were evaluated in a thermally fixed catalytic reaction system. The results indicated that the FeO$_x$/β-MnO$_2$ composite (Fe/Mn molar ratio of 0.3 and calcination temperature of 450 °C) had higher catalytic activity and a wider reaction temperature window compared with β-MnO$_2$. The water resistance and sulfur resistance of the catalyst were enhanced. It reached 100% NO conversion efficiency with an initial NO concentration of 500 ppm, a gas hourly space velocity of 45 000 h^{-1}, and a reaction temperature of 175–325 °C. The appropriate Fe/Mn molar ratio sample had a synergistic effect, affecting the morphology, redox properties, and acidic sites, and helped to improve the low-temperature NH$_3$-SCR activity of the composite catalyst.

1. Introduction

Excessive emissions of nitrogen oxides cause a series of environmental problems, such as the greenhouse effect,[1] acid rain,[2] photochemical smog,[3] etc. Furthermore, nitrogen oxides could enter the human body through inhalation, skin contact, and ingestion,[4] thus causing harm to humans.[5–7] Countries worldwide have set increasingly stringent emission standards to reduce NO$_x$ emissions.[8–10] Many technologies have been developed to reduce NO$_x$ emissions, among which selective catalytic reduction (SCR) with NH$_3$ as the reducing agent was the most mature and effective method, especially for stationary sources of NO$_x$ emissions. However, the application of this technology was limited due to most NH$_3$-SCR catalysts afforded activity merely at a high exhaust temperature.[11,12]

At present, the V$_2$O$_5$–WO$_3$/TiO$_2$ catalyst has been widely used in flue gas denitrification systems of thermal power plants. It had a narrow activation temperature window and was typically used in flue gases above 320 °C to ensure high NO$_x$ removal

activity.[13,14] Whereas its denitrification activity was inhibited while the flue gas temperature was lower. In addition, vanadium-containing catalysts were biotoxicity and prone to secondary contamination after deactivation or aging.[15] And it was listed on the China National List of Hazardous Chemicals in 2016.[16]

More recently, Mn-based catalysts attracted wide attention because of their outstanding NH$_3$-SCR activity.[17] Kapteijn et al.[18] found that MnO$_2$ had a higher SCR activity than other MnO$_x$. Meng et al.[19] found β-MnO$_2$ was the most catalytically active of the three crystalline types of MnO$_2$. Yang et al.[20] reported that β-MnO$_2$ had a good NH$_3$-SCR activity at 120 °C to 350 °C. However, it was weakly resistant to SO$_2$ and reacted with SO$_2$ to produce MnSO$_4$ to lose NH$_3$-SCR activity,[21] and need further strengthened in breadth and depth.

FeO$_x$ had been explored for NH$_3$-SCR reaction because of its environmentally friendly properties, satisfactory N$_2$ selectivity, and excellent tolerance of SO$_2$ at high temperatures.[22–24] Xie et al.[25] used Fe$_2$O$_3$-modified MnO$_2$/attapulgite (Mn–ATP) for NH$_3$-SCR and found that Fe$_2$O$_3$ modification could enhance the N$_2$ selectivity and resistance to H$_2$O/SO$_2$ of the catalyst. Qiu et al.[26] prepared S–MnFeCoCe/Ti/Si catalysts by Fe modification, which maintained high NO$_x$ conversion at 50 ppm SO$_2$ and 10 vol% H$_2$O. They also found that the presence of interactions between Mn oxide and Fe oxide enhanced the durability of the catalyst to sulfur and water.

In this study, using β-MnO$_2$ as a carrier and FeO$_x$ as modified additives, the FeO$_x$/β-MnO$_2$ composite catalyst was synthesized

[a]School of Resource and Environmental Engineering, Hefei University of Technology, Hefei 230009, P. R. China. E-mail: czzhu@hfut.edu.cn; Fax: +86 551 62901649; Tel: +86 551 62901523

[b]Institute of Atmospheric Environment & Pollution Control, Hefei University of Technology, Hefei 230009, P. R. China

[c]Key Laboratory of Nanominerals and Pollution Control of Anhui Higher Education Institutes, Hefei University of Technology, Hefei 230009, P. R. China

[d]Low Temperature Denitration Engineering Research Center of Anhui Province, Hefei 230001, P. R. China

by impregnation method. The denitrification activity of composite for SCR of NO$_x$ with NH$_3$ was systematically investigated. And the composite was characterized by X-ray diffraction, high-resolution electron microscope, temperature-programmed reduction of H$_2$ (H$_2$-TPR), temperature-programmed desorption of NH$_3$ (NH$_3$-TPD), and FTIR infrared spectroscopy, *etc.* techniques to explain the advantages of deNO$_x$ activity, water resistance, and sulfur resistance of the modified composite.

2. Experimental sections

2.1 Catalysts preparation

Synthetic β-MnO$_2$ was synthesized by the hydrothermal synthesis method.[27] MnSO$_4$ and an equal amount of (NH$_4$)$_2$S$_2$O$_8$ were dissolved in deionized water, then transferred into a Teflon-lined stainless steel autoclave, and reacted at 120 °C for 12 h. After the reaction was completed, the black solid product obtained by filtering was washed with derived ions to remove the possible ions in the final product. Finally, the product was dried in air at 120 °C.

The proportion of ferric nitrate and >60 mesh β-MnO$_2$ powders were dissolved in deionized water in turn and stirred for 1 h to form a uniform solution. The solution was heated to the slurry in a heating furnace and then transferred to a 100 °C oven for drying to obtain the precursors of FeO$_x$/β-MnO$_2$ composites.

The FeO$_x$/β-MnO$_2$ precursors were calcined at different temperatures for 2 h to obtain the catalysts. Based on the preparation conditions, they were noted as FeO$_x$(n)/β-MnO$_2$(z), where n represented the molar ratios of Fe and Mn and z represented the calcination temperatures. After cooling to room temperature, the catalyst was crushed and sieved, and 40–60 meshes of catalyst were selected for the NH$_3$-SCR activity test.

2.2 Catalysts characterization

The crystal structures of the catalysts were determined by the X-ray diffraction meter (XRD, D/Max-RB, Rigaku), Cu Kα radiation source, tube voltage 40 kV, tube current 80 mA, step length 0.02° s^{-1}, scanning range 10°–75°. The specific surface area and pore structure of the catalysts were determined by an automatic specific surface area analyzer (BET, NOVA3000e, Quantachrome, USA). The surface morphology of the samples was observed by high-resolution field emission scanning electron microscopy (SEM, Hitachi Regulus 8230, Japan). X-ray photoelectron spectrometer (XPS, Thermo ESCALAB250Xi, USA) was used to determine valence and element content (Al-Kα radiation, 1486.6 eV, and the C 1s line at 284.8 eV as the standard). H$_2$-TPR and NH$_3$-TPD were detected by the Autocue II 2920 chemisorbent of Mick Instrument Corporation in the United States. The surface functional groups of the catalysts were analyzed by Fourier transform infrared spectroscopy (FTIR, Bruker Vertex-70, Germany).

2.3 Catalytic performance test

The experiment of selective catalytic reduction of NO from ammonia gas was carried out using a thermostat bed catalytic reaction system. The system consisted of a flue gas mixing system, a catalytic fixed bed and a flue gas analysis system. The catalytic fixed bed was a cylindrical reactor with a Cr$_{18}$Ni$_9$Ti stainless steel shell on the outer layer and quartz cotton on the inner layer. The catalyst activity test was carried out on the catalytic fixed bed (quartz tube fixed bed with a diameter of 6 mm), and the catalytic reaction temperature was adjusted through the ceramic fiber tube heater, thermocouple, and temperature-programmed control device.

The gas distribution system had five gas branches, which were supplied by gas cylinders. The mass flow controller (Sevenstar, D07-7C, Beijing) was used to control the flow of each branch. The total gas flow was 300 mL min^{-1}. The simulated flue gas consisted of 0.05% NO, 0.05% NH$_3$, 3 vol% O$_2$, 10 vol% H$_2$O (when used), and 200/300 ppm SO$_2$ (when used), Ar as the balance gas. The water vapor was generated by the peristaltic pump together the heating tape and then passed into the gas line. The GHSV of 35 000 h^{-1} was selected.

The catalytic activity of the catalyst was measured by NO conversion (η_{NO}), and the NO concentration in the feed gas and tail gas was detected by flue gas analyzer (Madur GA-12plus, Austria).

$$\eta_{NO} = \frac{NO_{in} - NO_{out}}{NO_{in}} \times 100\% \tag{1}$$

where NO$_{in}$ and NO$_{out}$ represent the NO concentration of inlet and outlet, ppm, respectively.

3. Results and discussion

3.1 Catalytic performances

3.1.1 Optimum preparation conditions of the composite catalyst. The low-temperature deNO$_x$ performance of a series of catalysts was investigated in terms of two factors: the Fe/Mn molar ratios and the calcination temperatures. Fig. 1a showed the NO conversion of FeO$_x$(n)/β-MnO$_2$(400 °C) composite catalysts with different Fe/Mn molar ratios within the reaction temperature of 75 °C to 400 °C. The NO conversion of the catalyst loaded with iron oxide was significantly higher than that of β-MnO$_2$ at low temperatures (75–200 °C). The NH$_3$-SCR activity of the catalysts enhanced and then decreased with increasing the amount of loaded FeO$_x$, and the optimal Fe/Mn molar ratio was 0.3. This indicated that reasonable doping was beneficial to the catalytic reaction, while excessive doping had a rather unfavorable catalytic reaction.[28] The NO conversion of the FeO$_x$(0.3)/β-MnO$_2$(450 °C) composite catalyst can reach 100% at 175–325 °C with an hourly space velocity of gas (GHSV) of 35 000 h^{-1}

The calcination temperature could affect the SCR activity of the catalyst, and the catalytic activity of MnO$_2$ could be different at different calcination temperatures.[33] Fig. 1b showed the influence of different calcination temperatures on the NO conversion of FeO$_x$(0.3)/β-MnO$_2$(z) composite catalysts. When the calcination temperatures were 400 °C and 450 °C, the activity of the catalyst in the low-temperature section was very similar, but FeO$_x$(0.3)/β-MnO$_2$(450 °C) was slightly superior in the high-temperature section. When the calcination
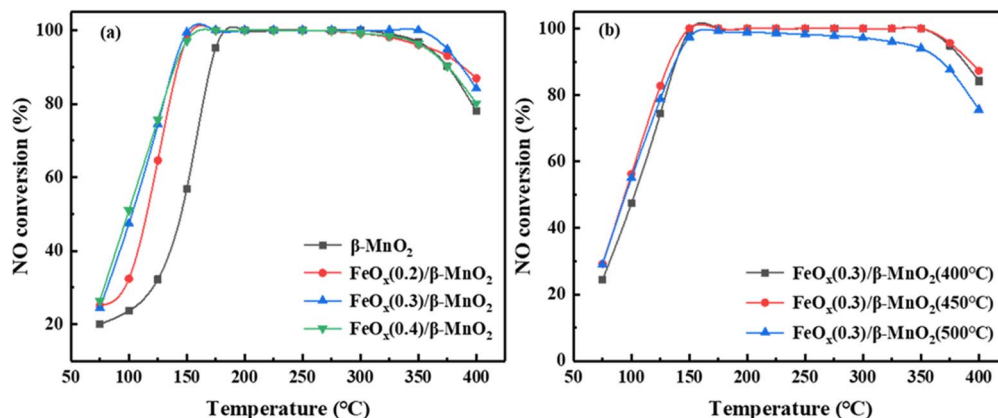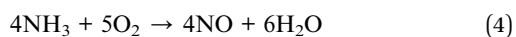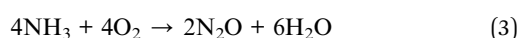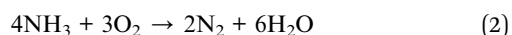
Fig. 1 Effect of (a) different Fe/Mn molar ratios and (b) different calcination temperatures on NO conversion efficiency of catalysts. Reaction conditions: 0.05% NO, 0.05% NH$_3$, 3 vol% O$_2$, Ar as the balance gas and GHSV of 35 000 h^{-1}.

temperature was 500 °C, the low-temperature SCR activity of FeO$_x$(0.3)/β-MnO$_2$(500 °C) was inferior to that of the composite catalysts calcined at other temperatures. This phenomenon tallied well with the activity test results of the catalysts prepared at different calcination temperatures.[34] In addition, along the reaction temperature increased from 325 °C to 400 °C, the activity of the FeO$_x$(0.3)/β-MnO$_2$(450 °C) composite catalyst decreased. It might be due to the Mn oxides and Fe oxides could reduce the activation energy of NH$_3$ oxidation reaction and promoted the oxidation of NH$_3$ to reduce the concentration of NH$_3$ in flue gas.[12,15] The reactions (2–4) could generate a certain amount of NO and a new pollutant N$_2$O, which could affect the denitrification effect of the catalyst.[7]

$$4NH_3 + 3O_2 \rightarrow 2N_2 + 6H_2O \tag{2}$$

$$4NH_3 + 4O_2 \rightarrow 2N_2O + 6H_2O \tag{3}$$

$$4NH_3 + 5O_2 \rightarrow 4NO + 6H_2O \tag{4}$$

Compared with other Mn-based and Fe-based catalysts from literature (Table 1), the prepared FeO$_x$(0.3)/β-MnO$_2$(450 °C) composite could maintain a high NO conversion over a wide temperature range and had a good industrial application prospect.

3.1.2 Effect of GHSV. GHSV affected the activity of the catalyst. The NO conversion of FeO$_x$(0.3)/β-MnO$_2$(450 °C) catalyst at different GHSV of simulated gases was shown in Fig. 2a. In the GHSV range of 15 000 h^{-1} to 45 000 h^{-1}, the NO conversion rate of FeO$_x$(0.3)/β-MnO$_2$(450 °C) still reached 100% at 175 °C to 325 °C. When the reaction temperature was below 175 °C, the NO conversion decreased slightly as the GHSV was increased. The deNO$_x$ efficiency of the catalyst decreased at temperatures above 325 °C under different GHSV, but the overall rule was not shown. From the above experiments, it was revealed that FeO$_x$(0.3)/β-MnO$_2$(450 °C) catalyst had a certain tolerance to higher GHSV and lower reaction temperature, which was more favorable in practice.

Table 1 The denitration efficiency of catalysts reported in the literature

Catalyst	Calcination	Reaction condition	NO conversion	Ref.
FeO$_x$/β-MnO$_2$	Impregnation	[NO] = [NH$_3$] = 500 ppm, 3% O$_2$ in Ar, GHSV = 35 000 h^{-1}	~100% (175–325 °C)	This work
MnO$_x$/α-Fe$_2$O$_3$	Impregnation	[NO] = [NH$_3$] = 500 ppm, 5% O$_2$ in Ar, GHSV = 72 000 h^{-1}	>90% (200–350 °C)	8
Fe–Mn/TiO$_2$(xPr)	Impregnation	[NO] = [NH$_3$] = 1000 ppm, 7% O$_2$ in N$_2$, GHSV = 30 000 h^{-1}	>95% (140–220 °C)	10
Fe–Mn/Ce$_1$Al$_2$	Co-precipitation	[NO] = [NH$_3$] = 500 ppm, 5% O$_2$ in Ar, GHSV = 30 000 h^{-1}	>90% (75–250 °C)	29
CeO$_2$–Fe$_2$O$_3$/Al$_2$O$_3$	Microwave hydrothermal	[NO] = [NH$_3$] = 500 ppm, 5% O$_2$ in N$_2$, GHSV = 6000 h^{-1}	>90% (200–300 °C)	30
Fe$_{0.8}$Mg$_{0.2}$O$_z$	Co-precipitation	[NO] = [NH$_3$] = 1000 ppm, 3.5% O$_2$ in N$_2$, GHSV = 6000 h^{-1}	>90% (250–350 °C)	31
Mn–Ce/Febeta	Incipient wetness co-impregnation	[NO] = 380 ppm, [NH$_3$] = 330 ppm, 10% O$_2$ in N$_2$, GHSV = 36 000 h^{-1}	>80% (180–500 °C)	32

© 2023 The Author(s). Published by the Royal Society of Chemistry
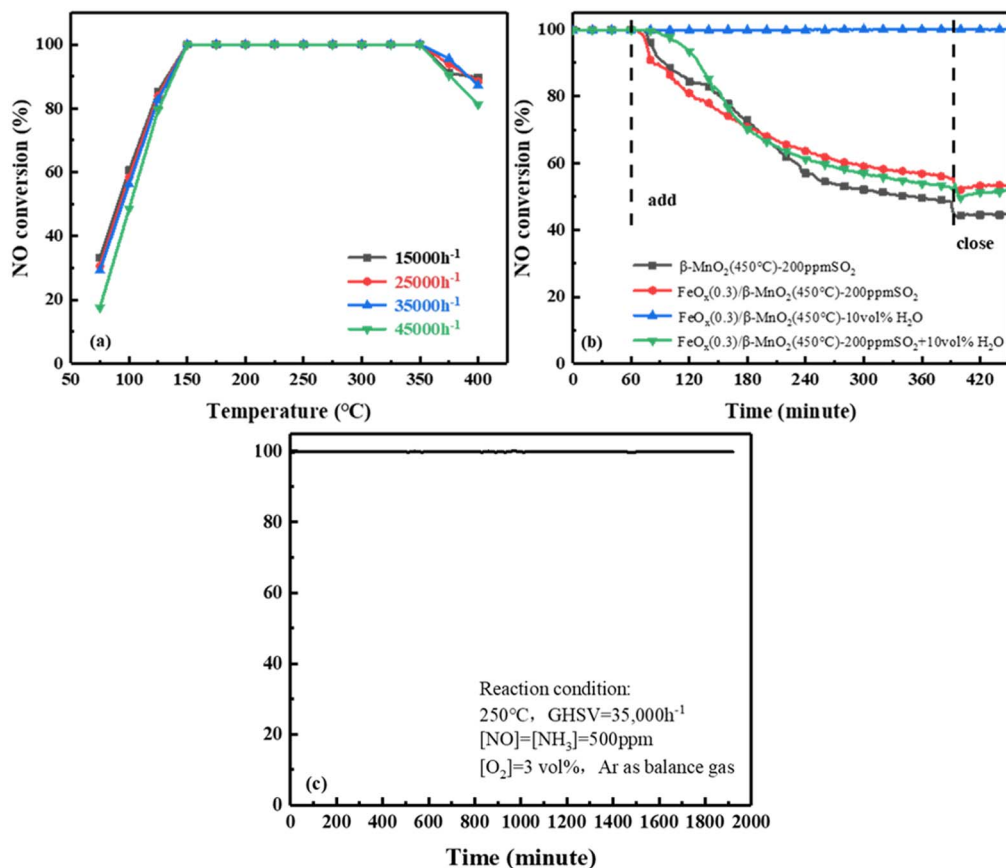
Fig. 2 (a) Effect of GHSV on NO conversion of FeO$_x$(0.3)/β-MnO$_2$(450 °C), (b) effect of H$_2$O and SO$_2$ on NO conversion of catalyst, (c) stability test of FeO$_x$(0.3)/β-MnO$_2$(450 °C) at 250 °C for 32 h.

3.1.3 H$_2$O and SO$_2$ tolerance. The combustion exhaust gas usually contained H$_2$O and some SO$_2$ when used in practice, this might lead to the deactivation of the SCR catalyst.[35] Fig. 2b showed the sulfur resistance and water resistance after 1 h stable reaction at 250 °C, simulated gases of 500 ppm NO, 500 ppm NH$_3$, and 3 vol% O$_2$, GHSV of 35 000 h^{-1}. When 200 ppm SO$_2$ was passed to β-MnO$_2$, the NO$_x$ conversion efficiency of β-MnO$_2$ dropped to 48% within 5.5 h and then stabilized at 44%. Compared with the performance of β-MnO$_2$(450 °C), the NO conversion rate of FeO$_x$(0.3)/β-MnO$_2$(450 °C) was reduced from 100% to 55% and stabilized at 53%. NO conversion without resume when SO$_2$ introduction was turned off, this might be due to the deposition of ammonium sulfate/bisulfate on the catalyst surface and the blocking of the active sites of the NH$_3$-SCR reaction.[36] The NO conversion rate on the catalyst was maintained at 100% when 10 vol% H$_2$O was passed into simulated gases, indicating that the catalyst had strong tolerance to H$_2$O.[37] When 200 ppm SO$_2$ and 10 vol% H$_2$O were simultaneously introduced into simulated gases, the NO conversion of the catalyst decreases to 52% and stabilized at 48%. Compared with 200 ppm SO$_2$ alone, the NO conversion rate had only a 5% decrease after 5.5 h. It indicated that SO$_2$ had a large effect on SCR activity and H$_2$O had a negligible effect, the coexistence of SO$_2$ and H$_2$O could have a certain synergistic effect on SCR activity. Therefore, compared with β-MnO$_2$, the

doping of Fe effectively improved the SO$_2$ resistance of the catalyst.[38,39]

3.1.4 Catalyst stability. The stability of a catalyst was a factor that affected its value in industrial applications. The FeO$_x$(0.3)/β-MnO$_2$(450 °C) catalyst was used for SCR reactions at 250 °C under GHSV of 35 000 h^{-1}, 500 ppm NO, 500 ppm NH$_3$, 3 vol% O$_2$, and Ar as balanced gas. As shown in Fig. 2c, the FeO$_x$(0.3)/β-MnO$_2$(450 °C) catalyst was consistently kept at 100% NO$_x$ conversion efficiency within 32 h. The results showed that FeO$_x$(0.3)/β-MnO$_2$(450 °C) catalyst had stable SCR performance and relatively high service life, which had certain practical application value.

3.2 Catalysts characterization

3.2.1 XRD analysis. The XRD spectra of β-MnO$_2$ with different calcination temperatures were shown in Fig. 3a. The hydrothermal synthesized MnO$_2$ samples showed different crystal shapes and structures at different temperatures. When calcined at temperatures of 400 °C and 450 °C, there were diffraction peaks at $2\theta = 28.84°$, 37.52°, 41.97°, 56.37°, 60.27°, 69.71°, 72.26° and 72.38° were attributed to β-MnO$_2$.[40] When the calcination temperature was 500 °C, the β-MnO$_2$ diffraction peaks disappeared, the diffraction peaks appeared at $2\theta = 23.3°$, 32.95°, 38.23°, 45.17°, 49.34°, 55.19°, and 65.80° were assigned to Mn$_2$O$_3$.[41] With the increase of calcination temperature, the
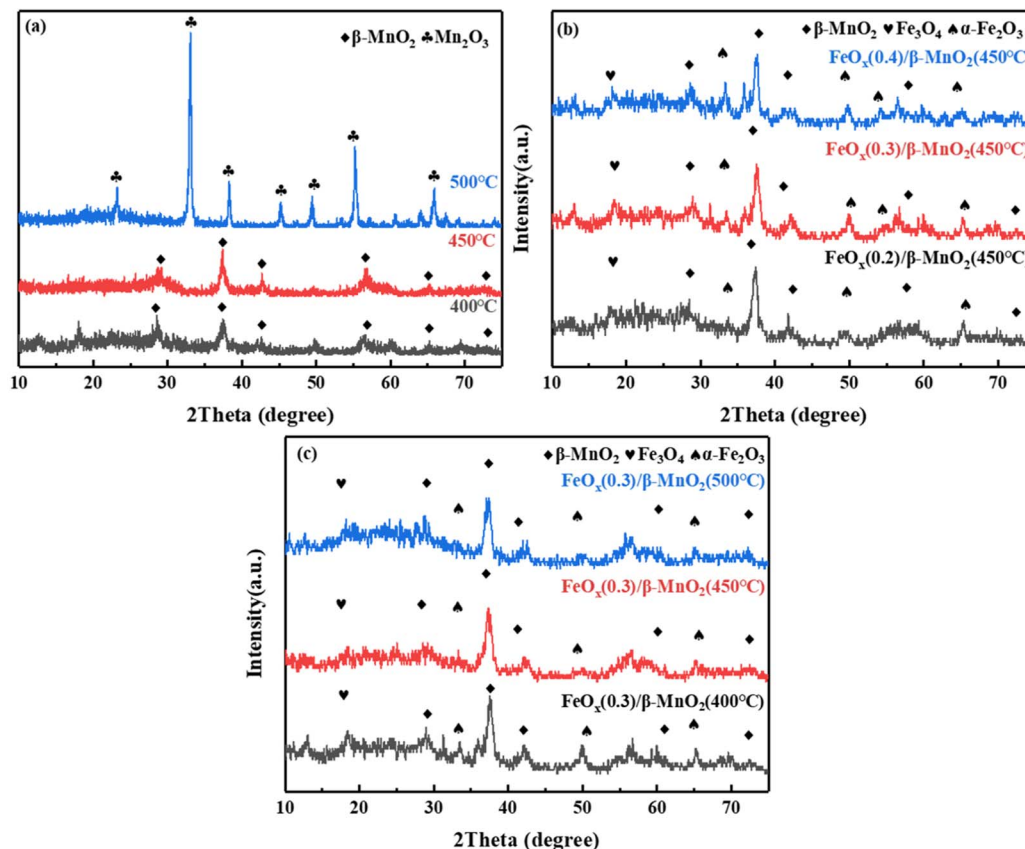
Fig. 3 XRD patterns of (a) β-MnO$_2$ at different calcination temperatures; (b) FeO$_x$(n)/β-MnO$_2$(450 °C) with different molar ratios of Fe/Mn; (c) FeO$_x$(0.3)/β-MnO$_2$ at different calcination temperatures.

sample changes from β-MnO$_2$ → Mn$_2$O$_3$. It should be the calcination at too high a temperature promoted the transition of the Mn valence from Mn^{4+} → Mn^{3+} in the sample.[33,42] Moreover, the reflections of samples enhanced with increasing calcination temperature, demonstrating an enhancement in crystallinity. It might be due to the sample will sinter at higher temperatures.

Ferric nitrate decomposes to FeO$_x$ at high temperatures, and its main components were α-Fe$_2$O$_3$ and Fe$_3$O$_4$ (Fig. 3b), the diffraction peaks of 2θ = 35.36° and 49.47° were attributed to Fe$_2$O$_3$, while 2θ = 18.29° was diffraction peak of Fe$_3$O$_4$.[43] With the increase of the Fe/Mn molar ratio, the peak intensity of β-MnO$_2$ decreased gradually. It indicated that the dispersion of β-MnO$_2$ increased with increasing Fe loading and it combined more fully with FeO$_x$, and favored by the formation of a large number of small particles of the active fraction, which promoted the fast SCR reaction.[44] However, with the increase of Fe content, the diffraction peak of α-Fe$_2$O$_3$ increased relatively
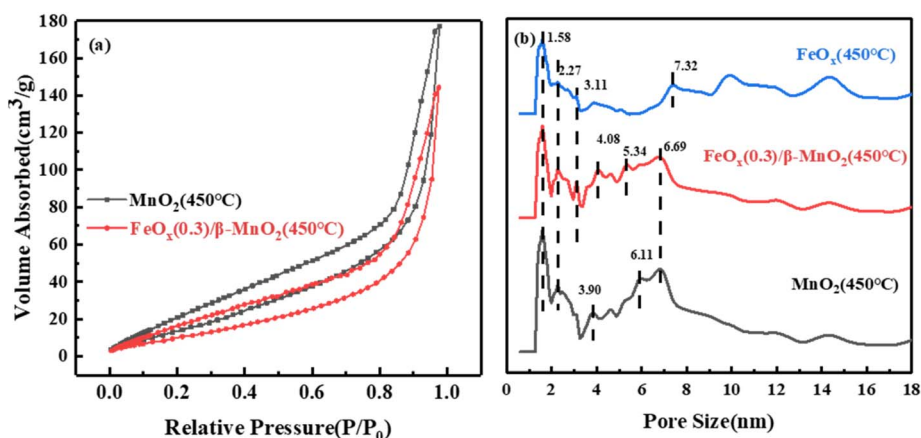

Fig. 4 (a) N$_2$ adsorption−desorption curve and (b) average pore size of catalysts.

Table 2 BET surface area, total pore volume, and average pore radius of β-MnO$_2$(450 °C), FeO$_x$(0.3)/β-MnO$_2$(450 °C), and FeO$_x$(450 °C)

Sample	Surface area/m^2 g^{-1}	Total pore volume/10^{-2} cm^3 g^{-1}	Average pore radius/nm
β-MnO$_2$(450 °C)	67.934	27.41	81.69
FeO$_x$(0.3)/β-MnO$_2$(450 °C)	45.905	22.31	97.22
FeO$_x$(450 °C)	23.788	19.89	167.26

while that of Fe$_3$O$_4$ decreased. It could be due to the transformation of part of Fe$_3$O$_4$ to Fe$_2$O$_3$. The co-existence of Fe^{2+} and Fe^{3+} could form an imbalance unsaturated chemical bonds, which could increase the amount of chemisorbed oxygen on the surface and improve the catalytic performance of the catalyst.[45] Combined with Fig. 1a and 3b, an appropriate Fe doping could produce tiny active particles and improve the catalytic activity, while excessive Fe doping was conducive to the formation of oxide masses, thus hindering the SCR reaction.[46]

The XRD diagrams of FeO$_x$(0.3)/MnO$_2$ at different calcination temperatures was shown in Fig. 3c. With the increasing of calcination temperature, the reflection peak intensity of MnO$_2$ increased and then decreased, while the reflection peak intensity of FeO$_x$ gradually weakened. The intensity of the reflection peak of β-MnO$_2$ was the largest when the calcination temperature was 450 °C. The intensity of FeO$_x$ reflection peak decreased, its dispersion increased and crystallinity became smaller, which was favorable to improve the catalytic performance.[47] The peak at $2\theta = 23.16°$ could be the reflection peak of Fe–Mn–O$_x$ formed by the reaction.[48] The formation of Fe–Mn–O$_x$ complexes was beneficial to improve the deNO$_x$ performance of the catalyst.[49] The efficiency of compound catalytic denitrification decreased at 500 °C due to the conversion of MnO$_2$ to Mn$_2$O$_3$, which was not favorable for deNO$_x$ reaction.[50]

3.2.2 N$_2$ adsorption and desorption. The specific surface area of the catalyst was important for adsorbing NH$_3$ and providing active sites.[51] The calcination temperature directly regulated the pore size distribution and pore structure of the catalyst, which in turn affected the performance of the catalyst.[52] The suitable temperature of calcination could effectively improve the low-temperature activity of the catalyst. The addition of Fe also had an effect on the morphology of the catalyst. Yin[53] reported that the specific surface area of catalysts were not the main factor affecting their deNO$_x$ activity. β-

MnO$_2$(450 °C) and FeO$_x$(450 °C) and the best catalyst FeO$_x$(0.3)/β-MnO$_2$(450 °C) were selected for N$_2$ adsorption and desorption experiments. The BET results of were shown in Fig. 4 and Table 2. The addition of Fe could reduce the surface area and total pore volume, and increase the average pore radius of the catalyst. In the N$_2$ adsorption–desorption isotherm, the adsorption branch did not coincide with the desorption branch, showing a hysteresis loop, which was attributed to the capillary condensation phenomenon that occurred in the process of N$_2$ low-temperature adsorption, indicating that there were mainly mesopores or micropores in the catalyst. According to the IUPAC classification, the overall isotherm showed class V, indicating the interaction between the sample surface and N$_2$ was weak.[54,55] The adsorption branch and desorption branch were almost parallel, and the hysteresis loop was H4 type, which indicated that there were smaller pores and larger pores on the sample surface.[55] It could be seen from the average pore size distribution diagram that Fe loading increased the content of 2.27 nm micropores and 3.11 nm micropores, which improved the average pore size of the catalyst. This meant that the catalyst samples had more mesopores, which contributed to the deNO$_x$ performance of the catalyst.[56]

3.2.3 SEM analysis. Hydrothermal β-MnO$_2$ showed a long and thin needle-like structure, which was stacked to form a solid structure (Fig. 5a). FeO$_x$ had a variety of morphologies, mostly granular and flaky structures that stacked together to form a three-dimensional structure (Fig. 5b), and existed with some agglomeration. FeO$_x$ loaded along needle-shaped MnO$_2$ in FeO$_x$(0.3)/β-MnO$_2$(450 °C) (Fig. 5c), which had a smoother rod structure with round particles at both ends. In contrast to β-MnO$_2$, the addition of Fe caused the original nanowire structure to break off and slowly assemble with FeO$_x$ to form rods. SEM images indicated that the morphologies of FeO$_x$/β-MnO$_2$ and β-
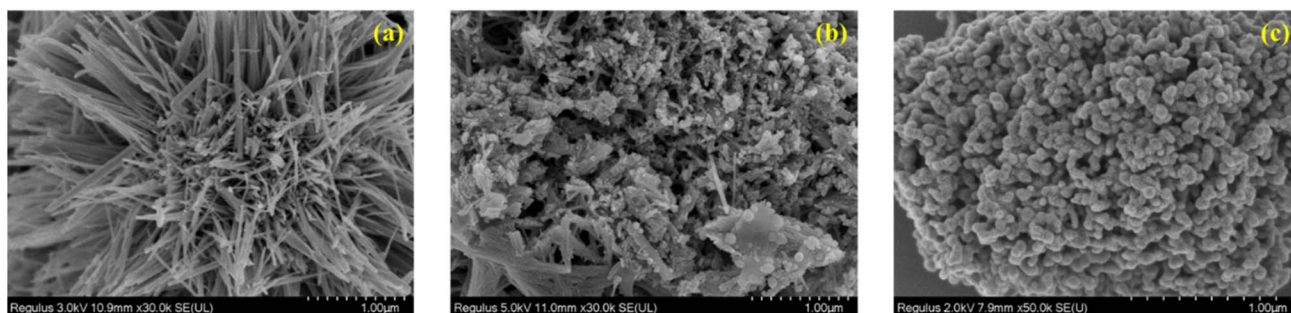
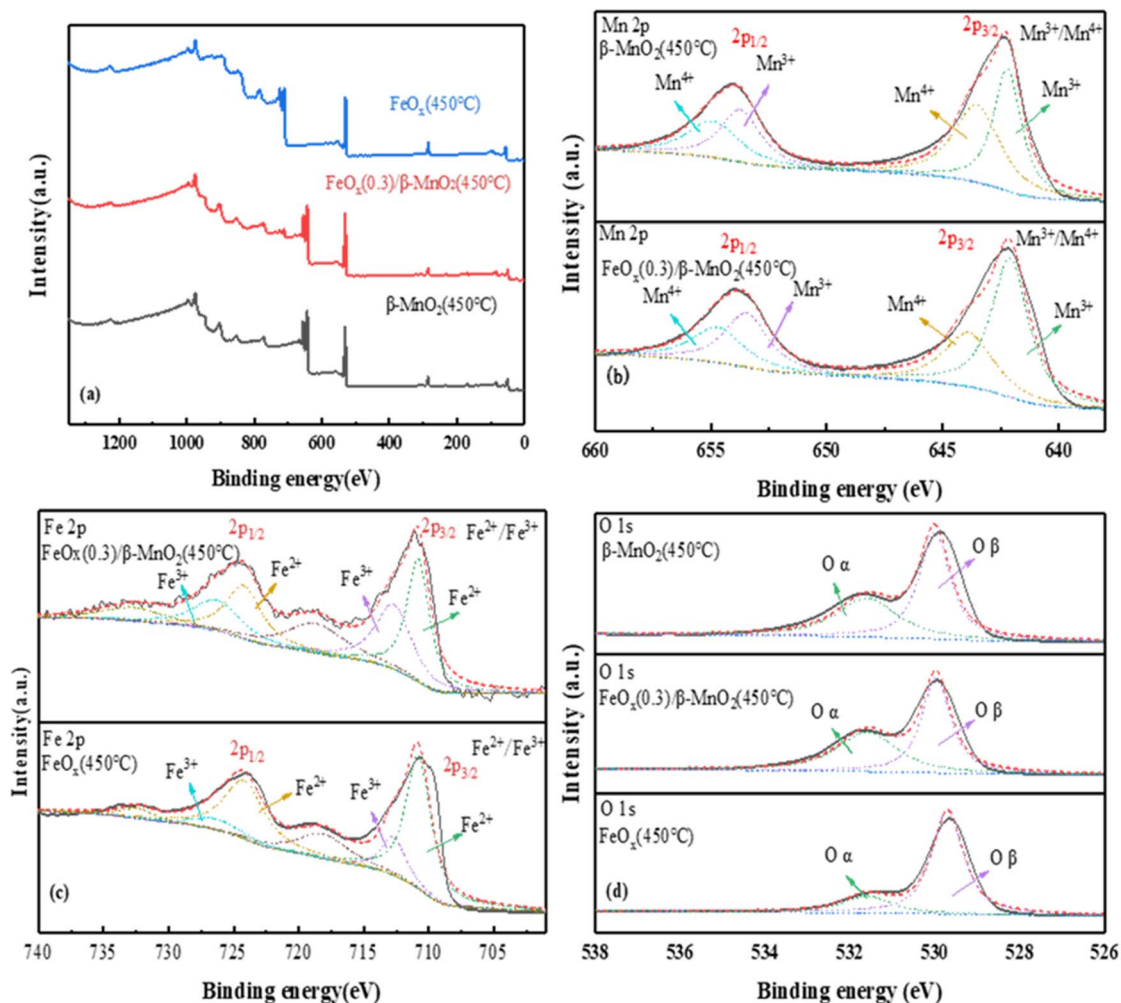**Fig. 5** SEM images of (a) β-MnO$_2$(450 °C), (b) FeO$_x$(450 °C), (c) FeO$_x$(0.3)/β-MnO$_2$(450 °C).

Fig. 6 XPS spectra of (a) total spectrum, (b) Mn 2p, (c) Fe 2p, (d) O 1s of MnO_2(450 °C), FeO_x(0.3)/β-MnO_2(450 °C), FeO_x(450 °C).

MnO_2 were significantly different, indicated that the doping of Fe had a strong influence on the β-MnO_2 nanowire. It demonstrated that the admixture of metal elements greatly changed the structure of β-MnO_2.[57] Combined with N_2 adsorption–desorption analysis, it showed that the sample was formed by the loose accumulation of spherical particles or flaky particles, with relatively narrow pore size distribution, good pore channel connectivity, and slit-like pore structure. And the FeO_x loaded was homogeneously dispersed, which contributed to the deNO$_x$ performance of the catalyst.
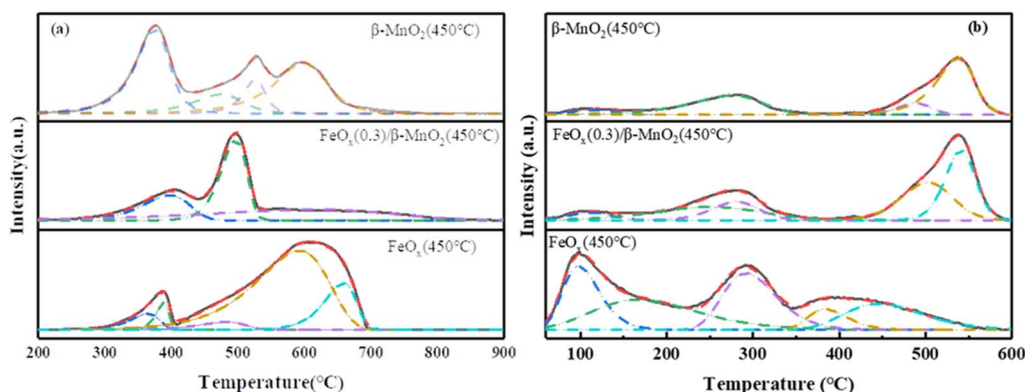

Fig. 7 (a) H_2-TPR and (b) NH_3-TPD profiles of β-MnO_2(450 °C), FeO_x(0.3)/β-MnO_2(450 °C), FeO_x(450 °C).
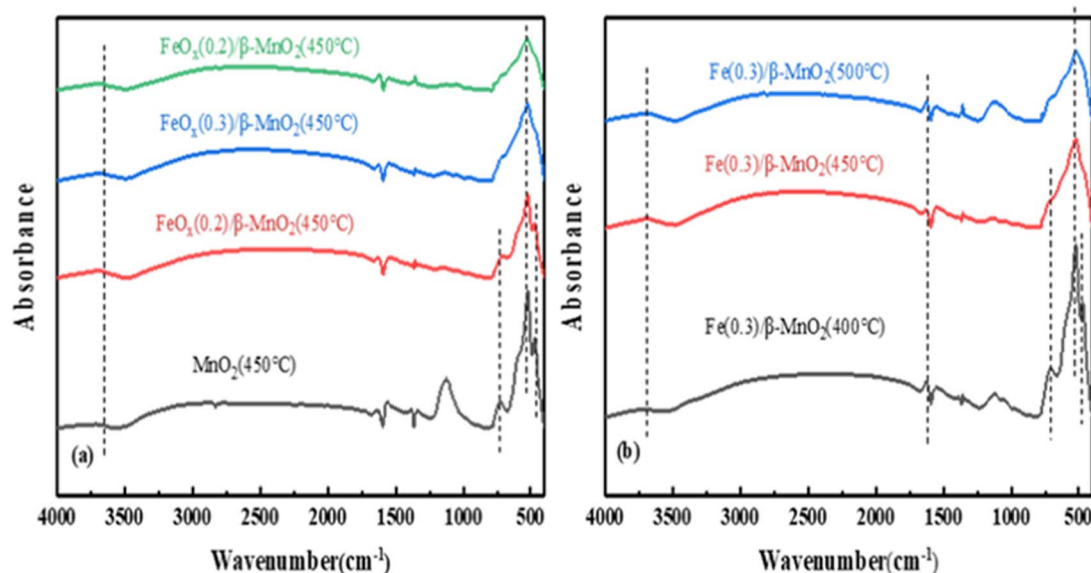
Fig. 8 FTIR spectra of (a) FeO_x/β-MnO_2(450 °C) at different Fe/Mn molar ratios and (b) FeO_x(0.3)/β-MnO_2 at different calcination temperatures.

3.2.4 XPS analysis. Fig. 6b showed the Mn 2p photoelectron spectrum. The peaks around 642 eV and 653 eV could be assigned to Mn $2p_{3/2}$ and Mn $2p_{1/2}$. They could be divided into Mn^{3+} (642.2 eV and 653.4 eV),[58] and Mn^{4+} (644.1 eV and 654.9 eV),[59] respectively.

The photoelectron spectrum of Fe 2p in the catalyst was shown in Fig. 6c. The four main peaks were Fe^{3+} (710 eV and 724 eV) and Fe^{2+} (712.7 eV and 726.3 eV); the weak peak at 718 eV was probably a satellite peak of Fe $2p_{3/2}$ and the weak peak at 732.7 eV a satellite peak of Fe $2p_{1/2}$.[60] The binding energies of 710.8 eV and 712.7 eV of Fe $2p_{3/2}$ and 724.2 eV and 726.3 eV of Fe $2p_{1/2}$ were attributed to Fe^{3+}.[61] The peak had a certain shift after the introduction of Fe, which may be the reaction of a small amount of Mn^{2+} with Fe^{3+} in the catalyst. The main reactions were: $Fe^{3+} + Mn^{2+} \rightarrow Fe^{2+} + Mn^{3+}$, $Fe^{3+} + Mn^{3+} \rightarrow Fe^{2+} + Mn^{4+}$. Mn^{3+} and Mn^{4+} had a great impact on the $deNO_x$ performance of the catalyst. Moreover, the higher the content of Mn^{3+} and Mn^{4+}, the better the redox performance for the conversion of NO.[45,62]

O 1s of the catalyst (Fig. 6d) showed a single peak of low binding energy 529.87–530.12 eV corresponded to lattice oxygen (O_β),[63] the high binding energy of 531.55–531.73 eV was the oxygen (O_α) $(O_\alpha$, mainly O^{2-}, O_2^{2-}).[64] The O_α had higher electron mobility and better catalytic activity.[65] Compared with the two raw materials, FeO_x(0.3)/β-MnO_2(450 °C) had the highest O_α content, indicating that it had better redox performance and higher activity. The addition of Fe increased lattice oxygen, improved oxygen vacancies, and enhanced the activity of surface oxygen, thereby contributed to NO_x and the formation of nitrate/nitrite products. Thus, it could conducive to fast SCR reaction and improved the denitrification effect in low-temperature environments.

3.2.5 H₂-TPR and NH₃-TPD analysis. In addition to the catalyst morphology, internal channels and other factors affecting the $deNO_x$ effect of the catalyst, the surface properties

of the catalysts also affected the $deNO_x$ activity of the catalyst. The surface properties of β-MnO_2, FeO_x(0.3)/β-MnO_2, and FeO_x samples were compared by H₂-TPR and NH₃-TPD, and the results were shown in Fig. 7.

The reduction peak of MnO_2 at 340–720 °C was mainly $MnO_2 \rightarrow Mn_2O_3 \rightarrow Mn_3O_4 \rightarrow MnO$, a series of Mn oxide transformations[66] (Fig. 7a). The reduction peak of the FeO_x sample at 388 °C corresponded to the reduction of Fe_2O_3 to Fe_3O_4, and the wide reduction peak at 450–850 °C was assigned to the process of $Fe_3O_4 \rightarrow FeO \rightarrow Fe$.[67] The maximum peak area of the FeO_x(0.3)/β-MnO_2 sample was obtained at 488 °C, which indicated that the consumption of H₂ of the catalyst sample was the largest at 488 °C. The main reaction at this temperature was the conversion of Mn oxide, which was the conversion of MnO_2 to Mn_2O_3. FeO_x(0.3)/β-MnO_2 compared to the β-MnO_2 sample had an earlier reduction peak position, lower reduction temperature, and larger peak value, which indicated that the addition of FeO_x led to a stronger redox capacity of the catalyst.[68] There were overlapping reduction peaks of $Fe_2O_3 \rightarrow Fe_3O_4$ and $MnO_2 \rightarrow Mn_2O_3$ at about 375 °C. There were reduction peaks of $Fe_2O_3 \rightarrow Fe_3O_4$ and $MnO_2 \rightarrow Mn_2O_3$ overlapping at about 375 °C. The reduction peaks at 450–600 °C were mainly $Mn_3O_4 \rightarrow MnO$ and $Fe_3O_4 \rightarrow FeO$.[28] The addition of FeO_x made β-MnO_2 have a stronger redox capacity, improved the oxygen storage capacity of the catalyst, and enhanced the activity of the catalyst.

The adsorption of NH₃ at the acid site was a key step in the NH₃-SCR reaction, the strength and density of the acid site closely affected the denitrification performance of the catalyst.[69] The NH₃-TPD spectral diagram of the sample (Fig. 7b) showed that the desorption peak around 110 °C was attributed to the physical adsorption of NH₃.[8] The desorption peaks at 160–220 °C and 200–350 °C could belong to NH_4^+ binding at the weak Brønsted acid site and NH_4^+ binding at strong the Brønsted acid site,[70] respectively. 410–600 °C could be attributed to the adsorption of NH₃ by strong Lewis acid site.[71] The desorption

peak of β-MnO$_2$ samples was small in the range of 160–350 °C, and the absorption peak of FeO$_x$(0.3)/β-MnO$_2$ samples increased in the range of 150–350 °C, indicating that the doping of FeO$_x$ increased the Brønsted acid site on the catalyst surface. Brønsted acid sites could affect the low-temperature denitrification efficiency of the catalyst, and increased amount of Brønsted acid sites could enhance the adsorption of NH$_3$, thus improving the low-temperature denitrification efficiency, which was consistent with the results of denitrification experiments.[72] In addition, doping Fe oxide also expanded the desorption peak area of the sample, which increased the acid site on the sample surface and improved the adsorption capacity of the catalyst for NH$_3$.[73]

3.2.6 FTIR spectral analysis. Fig. 8 showed the FT-IR spectra of FeO$_x$/β-MnO$_2$ samples with different molar ratios and FeO$_x$(0.3)/β-MnO$_2$ samples with different calcination temperatures. The wavelength below 1000 cm^{-1} was usually due to the interatomic vibration caused by the hydroxides and oxides of nanoparticles.[74] The absorption peak within 470 cm^{-1} and 730 cm^{-1} could be attributed to the presence of M–O nanostructures and Fe–O nanostructures, respectively.[75,76] In particular, 466 cm^{-1} could belong to the O–Mn–O bond,[76] the wavelength of 1630 cm^{-1} represented the presence of adsorbed water, and the absorption peak of 3600 cm^{-1} could be attributed to Brønsted acid 2 site.[77] The absorption peaks at 466 cm^{-1} and 723 cm^{-1} gradually disappeared with the increase of Fe loading. It could be due to the disappearance of some Mn–O nanostructures caused by the introduction of Fe. And the calcination temperature had a less effect on the functional groups of the catalyst (Fig. 8b). The variation of the absorption peak at 1120 cm^{-1} could be attributed to the formation of composite oxides between Fe species and Mn species.

Based on the above characterization analysis, the denitration mechanism of the catalyst could be Langmuir–Hinshelwood mechanism.[78] The doping of Fe increased Brønsted acid sites on the catalyst surface, improved the redox ability,[79] and improved the deNO$_x$ performance of the composite catalyst.

4. Conclusion

FeO$_x$/β-MnO$_2$ composite catalyst were prepared with impregnation method by using β-MnO$_2$ as the carrier and FeO$_x$ in mixed valence state as the modified additive. The results showed that the FeO$_x$/β-MnO$_2$ composite catalyst with Fe/Mn molar ratio of 0.3 and calcination temperature of 450 °C had an excellent low-temperature activity, a superior resistance to H$_2$O and good resistance to SO$_2$ compared with β-MnO$_2$. When NO initial concentration of 500 ppm, a gas hourly space velocity of 45 000 h^{-1}, and a reaction temperature of 175–325 °C, NO conversion efficiency could reach 100%. Adding an appropriate amount of FeO$_x$ could improve the valence distribution of Mn and Fe, increased the number of acid sites, and enhanced the redox ability of the composite catalyst.

Author contributions

Bo Du: investigation, conceptualization, methodology, data curation, formal analysis, visualization, writing – original draft.

Yuting Hu: investigation, data curation, Ting Cheng: methodology, formal analysis. Zhaozhong Jiang: investigation, visualization. Zhenzhen Wang: validation, methodology. Chengzhu Zhu: supervision, methodology, conceptualization, validation, resources, writing – review & editing, project administration.

Conflicts of interest

The authors declared that they have no conflicts of interest to this work.

Acknowledgements

References

1 Z. Si, D. Weng, X. Wu, G. Li and J. Li, *Sci. Technol. Rev.*, 2009, **27**, 87–95.

2 A. M. Mocioiu, D. I. Baila, C. I. Codrea and O. C. Mocioiu, *Inorganics*, 2022, **10**, 10040044.

3 Y. J. Zhang, M. M. Cheng, J. Gao and J. L. Li, *J. Environ. Sci.*, 2023, **123**, 545–559.

4 R. Balasubramanian, X. Gao, S. R. Hatakeyama, J. H. Hwang and C. J. Tsai, *Aerosol Air Qual. Res.*, 2017, **17**, 351–355.

5 H. Q. Wang, J. T. Zhou, X. Li, Q. Ling, H. Y. Wei, L. Gao, Y. He, M. Zhu, X. Xiao, Y. J. Liu, S. Li, C. L. Chen, G. T. Duan, Z. M. Peng, P. L. Zhou, Y. F. Duan, J. B. Wang, T. Z. Yu, Y. X. Yang, J. G. Wang, Z. Zhou, H. Q. Gui and Y. J. Ding, *J. Environ. Sci.*, 2023, **123**, 367–386.

6 H. Y. Liang, X. Zhou, Y. Q. Zhu, D. W. Li, D. R. Jing, X. L. Su, P. H. Pan, H. Liu and Y. Zhang, *Environ. Res.*, 2023, **218**, 114996.

7 X. F. Wang, Y. Xu, M. Y. Qin, Z. Zhao, X. F. Fan and Q. B. Li, *J. Colloid Interface Sci.*, 2022, **622**, 1–10.

8 H. M. Zhou, L. L. Qian, T. Cheng, B. Du, F. J. Xia and C. Z. Zhu, *J. Chem.*, 2022, **2022**, 5049161.

9 Y. Wu, S. J. Zhang, J. M. Hao, H. Liu, X. M. Wu, J. N. Hu, M. P. Walsh, T. J. Wallington, K. M. Zhang and S. Stevanovic, *Sci. Total Environ.*, 2017, **574**, 332–349.

10 X. X. Hou, H. P. Chen, Y. H. Liang, X. Yang and Y. L. Wei, *Catal. Lett.*, 2020, **150**, 1041–1048.

11 A. A. S. Goncalves, F. Ciesielczyk, B. Samojeden and M. Jaroniec, *J. Hazard. Mater.*, 2021, **401**, 123413.

12 Z. W. Shi, Q. G. Peng, J. Q. E, B. Xie, J. Wei, R. X. Yin and G. Fu, *Fuel*, 2023, **331**, 125885.

13 W. J. Liu, Y. F. Long, S. N. Liu, Y. Y. Zhou, X. Tong, Y. J. Yin, X. Y. Li, K. Hu and J. J. Hu, *J. Taiwan Inst. Chem. Eng.*, 2022, **138**, 104472.

14 Z. W. Zheng, X. S. Du, X. Wang, Y. G. Liu, K. L. Chen, P. Lu, V. Rac and V. Rakic, *Fuel*, 2023, **333**, 126443.

15 X. F. Wang, Z. Zhao, Y. Xu and Q. B. Li, *Appl. Surf. Sci.*, 2021, **569**, 151047.

16 H. J. Chen, R. Wang, Y. L. Yang, X. L. Shi, S. Y. Lu and Z. G. Chen, *Prog. Nat. Sci.: Mater. Int.*, 2021, **31**, 858–864.

17 G. Y. Xu, X. L. Guo, X. X. Cheng, J. Yu and B. Z. Fang, *Nanoscale*, 2021, **13**, 7052–7080.

18 F. Kapteijn, L. Singoredjo, A. Andreini and J. Moulijn, *Appl. Catal., B*, 1994, **3**, 173–189.

19 H. Meng, X. Wu, C. Ci, Q. Zhang and Z. Li, *Prog. React. Kinet. Mech.*, 2018, **43**, 219–228.

20 R. Yang, S. Peng, B. Lan, M. Sun, Z. Zhou, C. Sun, Z. Gao, G. Xing and L. Yu, *Small*, 2021, **17**, 2102408.

21 C. M. Li, X. L. Zhang, Y. J. Li, L. X. Sun, L. Huangfu, J. L. Li, S. Q. Gao and J. Yu, *Fuel*, 2023, **334**, 126590.

22 L. J. Jiang, Y. Liang, W. Z. Liu, H. L. Wu, T. Aldahri, D. S. Carrero and Q. C. Liu, *J. Environ. Chem. Eng.*, 2021, **9**, 106360.

23 S. Y. Xu, L. T. Yin, H. M. Wang, L. Y. Gao, X. Y. Tian, J. J. Chen, Q. L. Zhang and P. Ning, *Sep. Purif. Technol.*, 2022, **300**, 121824.

24 V. Zabihi, M. H. Eikani, M. Ardjmand, S. M. Latifi and A. Salehirad, *Environ. Sci. Pollut. Res.*, 2021, **28**, 39159–39167.

25 A. Xie, Y. Tao, X. Jin, P. Gu, X. Huang, X. Zhou, S. Luo, C. Yao and X. Li, *New J. Chem.*, 2019, **43**, 2490–2500.

26 L. Qiu, D. K. Li, H. L. Li, Z. Y. Ren, Z. Y. Zhu, F. Ouyang and M. X. Guo, *Chemosphere*, 2022, **302**, 134740.

27 X. Wang and Y. Li, *J. Am. Chem. Soc.*, 2002, **124**, 2880–2881.

28 T. Wang, Z. T. Wan, X. C. Yang, X. Y. Zhang, X. X. Niu and B. M. Sun, *Fuel Process. Technol.*, 2018, **169**, 112–121.

29 L. L. Li, J. W. Ji, W. Tan, W. Song, X. Wang, X. Q. Wei, K. Guo, W. Y. Zhang, C. J. Tang and L. Dong, *J. Rare Earths*, 2022, **40**, 1454–1461.

30 K. Zhang, J. J. Wang, P. F. Guan, N. Li, Z. J. Gong, R. Zhao, H. J. Luo and W. F. Wu, *Mater. Res. Bull.*, 2020, **128**, 110871.

31 L. T. Xu, S. L. Niu, C. M. Lu, Q. Zhang and J. Li, *Fuel*, 2018, **219**, 248–258.

32 A. I. Mytareva, D. A. Bokarev, D. S. Krivoruchenko, G. N. Baeva, A. Y. Belyankin and A. Y. Stakheev, *Top. Catal.*, 2019, **62**, 86–92.

33 Y. Jiang, G. Cheng, R. N. Yang, H. F. Liu, M. Sun, L. Yu and Z. F. Hao, *J. Solid State Chem.*, 2019, **272**, 173–181.

34 X. N. Huang, Y. F. Duan, J. L. Meng, X. Wu, W. M. Zhao, P. Hu, C. Zhu, H. Q. Wei and Y. G. Ma, *Asia-Pac. J. Chem. Eng.*, 2021, **16**, e2587.

35 K. J. Lee, P. A. Kumar, M. S. Maqbool, K. N. Rao, K. H. Song and H. P. Ha, *Appl. Catal., B*, 2013, **142**, 705–717.

36 S. P. Ding, F. D. Liu, X. Y. Shi, K. Liu, Z. H. Lian, L. J. Xie and H. He, *ACS Appl. Mater. Interfaces*, 2015, **7**, 9497–9506.

37 C. Z. Wang, Y. G. Zhao, C. Zhang, X. Yan and P. Cao, *Res. Chem. Intermed.*, 2018, **44**, 3135–3150.

38 G. S. Qi and R. T. Yang, *Appl. Catal., B*, 2003, **44**, 217–225.

39 Y. F. Liu, B. Z. Zhu, J. Y. Chen, Y. L. Sun and M. G. Xu, *J. Mater. Sci.*, 2022, **57**, 18468–18485.

40 Z. H. Ji, D. Dong, H. L. Guo, Y. M. Chai, Y. P. Li, Y. Q. Liu and C. G. Liu, *Mater. Chem. Phys.*, 2012, **136**, 831–836.

41 P. M. Kharade, S. B. Kulkarni and D. J. Salunkhe, *Chin. J. Phys.*, 2017, **55**, 1684–1689.

42 A. C. Zhang, Z. H. Zhang, J. J. Chen, W. Sheng, L. S. Sun and J. Xiang, *Fuel Process. Technol.*, 2015, **135**, 25–33.

43 C. Yang, J. Yang, Q. R. Jiao, Y. M. Tian, Q. C. Liu, S. Ren and J. L. Li, San Diego, CA, 2020.

44 R. P. Velez, I. Ellmers, H. M. Huang, U. Bentrup, V. Schunemann, W. Grunert and A. Bruckner, *J. Catal.*, 2014, **316**, 103–111.

45 X. L. Tang, C. Z. Wang, F. Y. Gao, Y. L. Ma, H. H. Yi, S. Z. Zhao and Y. S. Zhou, *J. Environ. Chem. Eng.*, 2020, **8**, 104399.

46 M. Schwidder, S. Heikens, A. De Toni, S. Geisler, M. Berndt, A. Bruckner and W. Grunert, *J. Catal.*, 2008, **259**, 96–103.

47 J. H. Kwak, R. G. Tonkyn, D. H. Kim, J. Szanyi and C. H. F. Peden, *J. Catal.*, 2010, **275**, 187–190.

48 A. Cetin, A. M. Onal and E. N. Esenturk, *J. Mater. Res.*, 2019, **34**, 3231–3239.

49 F. T. Xia, Z. X. Song, X. Liu, X. Liu, Y. H. Yang, Q. L. Zhang and J. H. Peng, *Res. Chem. Intermed.*, 2018, **44**, 2703–2717.

50 D. H. Wang, H. Li, N. Dong and S. E. Hui, *J. Environ. Eng.*, 2021, **147**, 04021039.

51 S. Z. Xie, L. L. Li, L. J. Jin, Y. H. Wu, H. Liu, Q. J. Qin, X. L. Wei, J. X. Liu, L. H. Dong and B. Li, *Appl. Surf. Sci.*, 2020, **515**, 146014.

52 L. Xu, S. Niu, C. Lu, Q. Zhang and J. Li, *Fuel*, 2018, **219**, 248–258.

53 S. Yin, B. Zhu, Y. Sun, Z. Zi, Q. Fang, G. Li, C. Chen, T. Xu and J. Li, *Asia-Pac. J. Chem. Eng.*, 2018, **13**, e2231.

54 Y. Tian and J. Z. Wu, *AIChE J.*, 2018, **64**, 286–293.

55 M. Thommes, K. Kaneko, A. V. Neimark, J. P. Olivier, F. Rodriguez-Reinoso, J. Rouquerol and K. S. W. Sing, *Pure Appl. Chem.*, 2015, **87**, 1051–1069.

56 Z. Q. Gong, S. L. Niu, Y. J. Zhang and C. M. Lu, *Mater. Res. Bull.*, 2020, **123**, 110693.

57 A. K. Worku, D. W. Ayele and N. G. Habtu, *Mater. Today Adv.*, 2021, **9**, 100116.

58 S. J. Yang, C. Z. Wang, J. H. Li, N. Q. Yan, L. Ma and H. Z. Chang, *Appl. Catal., B*, 2011, **110**, 71–80.

59 L. H. Wei, X. Y. Li, J. C. Mu, X. Y. Wang, S. Y. Fan, Z. F. Yin, M. O. Tad and S. M. Liu, *ACS Sustainable Chem. Eng.*, 2020, **8**, 17727–17739.

60 J. X. Sun, H. Chen, H. Wu, C. S. Zhou and H. M. Yang, *Can. J. Chem. Eng.*, 2019, **97**, 2498–2504.

61 W. Ahn, M. G. Park, D. U. Lee, M. H. Seo, G. P. Jiang, Z. P. Cano, F. M. Hassan and Z. W. Chen, *Adv. Funct. Mater.*, 2018, **28**, 1802129.

62 Z. J. Zhou, X. W. Liu, C. P. Li, Y. D. Yang, J. Xu and M. H. Xu, *Fuel*, 2020, **277**, 118230.

63 M. Y. Qiu, S. H. Zhan, H. B. Yu, D. D. Zhu and S. Q. Wang, *Nanoscale*, 2015, **7**, 2568–2577.

64 X. M. Zhou, X. Y. Huang, A. J. Xie, S. P. Luo, C. Yao, X. Z. Li and S. X. Zuo, *Chem. Eng. J.*, 2017, **326**, 1074–1085.

65 D. H. Wang, Q. Yao, C. H. Mou, S. E. Hui and Y. Q. Niu, *Fuel*, 2019, **254**, 115719.

66 X. B. Wang, J. Zhou, T. Zhao, K. T. Gui, J. Wang and H. R. Thomas, *J. Environ. Sci.*, 2020, **88**, 237–247.

67 N. S. Portillo-Velez and R. Zanella, *Chem. Eng. J.*, 2020, **385**, 123848.

68 X. Fang, Y. J. Liu, L. Z. Chen and Y. Cheng, *Chem. Eng. J.*, 2020, **399**, 125798.

69 X. Wu, H. Meng, Y. L. Du, J. N. Liu, B. H. Hou and X. M. Xie, *J. Catal.*, 2020, **384**, 72–87.

70 M. Hosseinpour, M. Akizuki, A. Yoko, Y. Oshima and M. Soltani, *Microporous Mesoporous Mater.*, 2020, **292**, 109708.

71 S. Yan, G. Ying, S. Wei and W. Yajuan, *Trans. Tianjin Univ.*, 2017, **23**, 35–42.

72 S. G. Zhang, C. Zhang, Q. Wang and W. S. Ahn, *Ind. Eng. Chem. Res.*, 2019, **58**, 22857–22865.

73 T. Wang, X. Y. Zhang, J. Liu, H. Z. Liu, Y. H. Guo and B. M. Sun, *Fuel Process. Technol.*, 2018, **178**, 53–61.

74 M. N. Uddin, G. C. Saha, M. A. Hasanath, M. T. Rahman and M. M. Rashid, *Advances in Civil Engineering: Select Proceedings of ICACE 2020. Lecture Notes in Civil Engineering*, edn 184, 2022, pp. 45–54, DOI: **10.1007/978-981-16-5547-0_5**.

75 A. Rai and A. K. Thakur, *Ceram. Int.*, 2017, **43**, 13828–13838.

76 S. Rada, A. Dehelean, M. Culea and E. Cule, *Spectrochim. Acta, Part A*, 2011, **79**, 320–324.

77 G. S. Qi, J. E. Gatt and R. T. Yang, *J. Catal.*, 2004, **226**, 120–128.

78 C. G. Zhang, T. H. Chen, H. B. Liu, D. Chen, B. Xu and C. S. Qing, *Appl. Surf. Sci.*, 2018, **457**, 1116–1125.

79 B. Z. Zhu, Q. L. Fang, Y. L. Sun, S. L. Yin, G. B. Li, Z. H. Zi, T. T. Ge, Z. C. Zhu, M. X. Zhang and J. X. Li, *J. Mater. Sci.*, 2018, **53**, 11500–11511.